Chapter 2

Dynamic magnetic responses in ensemble of anisotropic nanosystems

2.1 INTRODUCTION

Magnetic nanoparticles show enchanting spin dynamics behaviour because of their inherent behaviour [1–7]. If strong demagnetizing interaction dominates the primary MNPs in their ensemble, then magnetization is found to be interdependent [8,9]. In the presence of competing interparticle interactions in MNPs, arbitrarily aligned anisotropy axes result in collective spin freezing [9–12]. Consequently, prominent nonergodic behaviours with magnetically frustrated states [13–17] evolve at a definite temperature because of collective spin freezing, in spite of individual spin blocking [18, 19]. If the temperature comes below freezing temperature, MNPs show out-of-equilibrium spin dynamics with continuous slowing of spin. However, in such a scenario, the system is incapable of achieving its thermodynamic equilibrium state [20,21]. The nonequilibrium spin-glass states exhibit MME, ageing, and rejuvenation behaviours [22–28].

The non-ergodic behavious of an ensemble of MNPs rely on the MNPs' concentration, their interfacial exchange interaction, and the strength of dipolar interaction [1,2, 29–34]. The basic mechanism of spin dynamics in the ensemble of MNPs is an important subject to extensively understand the dynamic magnetic responses. As discussed in Chapter 1, Dormann-Bessais-Fiorani (DBF) [47, 48] and Mørup-Tronc (MT) [49] theories generally explain the impact of dipolar interaction on spin relaxation, but with few contradictory conclusions. As per the DBF model, spins show slower relaxation with the enhancement in dipolar strength, while the MT model explains faster spin relaxation having higher

K. Konwar, S.D. Kaushik, D. Sen, and P. Deb, Dynamic spin freezing and magnetic memory effect in ensembles of interacting anisotropic magnetic nanoparticles, *Physical Review B*, 102:174449, 2020.

dipolar interaction. If the effect of MNP geometrical arrangement in the ensemble is considered with partial alignment of easy axes, successive interchange between domain alignment and geometric pattern in the ensemble can further regulate the magnetic anisotropy, which can lead to spin frustration. Additionally, while considering the interacting anisotropic $ZnFe_2O_4$, the demagnetizing field strength can affect the anisotropic energy landscape, resulting in few modulations in the non-ergodic behaviour of the ensemble.

In this chapter, the demagnetizing field is considered to understand the dynamic magnetic responses in an ensemble of anisotropic $ZnFe_2O_4$ nanorods and their respective modulation in MME is addressed. Two varied organization geometries are considered, a compact ensemble of Zinc Ferrite (CEZF) and a hollow core ensemble of Zinc Ferrite (HCEZF)with different spatial arrangements of MNPs having dipolar strength. The nonequilibrium spin dynamics are revealed with the aid of both dc and ac magnetization study and dominance of cluster SG state is evident in CEZF and HCEZF. The structural correlation is also addressed in this chapter. With varied geometry of ensembles, along with easy axes alignment, the demagnetizing interaction-dependent MME effect is addressed.

2.2 EXPERIMENTAL DETAILS

The synthesis technique of CEZF and HCEZF of $ZnFe_2O_4$ nanorods is executed with the aid of a template-free solvothermal synthesis process with slight modifications [50]. The required precursors are obtained from Zenith, India, and used. The required stoichiometric zinc acetate dihydrate amount is considered with ferric nitrate nonahydrate, and allowed to stir in a glycerol and isopropyl-alcohol solution. A reddish solution is achieved, which is allowed to be autoclaved for a period of 12 h for CEZF and 21 h for HCEZF at 180 °C. A greenish-yellow product is collected, by performing centrifugation as well as drying. Then the achieved powder is calcined for 2 h at 400 °C and we attain a

dark brown powder. We perform Powder X-ray-diffraction (PXRD) study for microstructural confirmation (with Rigaku diffractometer having a radiation source of Cu-Kα following rate of 1°/min). Further, High-resolution transmission electron microscopy (HRTEM) images are taken considering a JEOL-JEM-2100 Plus model of Electron Microscope of 200 kV. For structural characterizations, Small-Angle X-ray Scattering (SAXS) is measured by using SAXS instrument having a point collimator with wavelength λ of 0.15 nm. For medium-resolution small-angle neutron-scattering (MSANS), neutron wavelength~0.312 nm is used using a double crystal-based MSANS instrument. For magnetic analyses, a vibrating sample magnetometer of Quantum Design Dynacool Physical Property Measurement System (PPMS) is used, in a field range of −9 to +9 T.

2.3 RESULTS AND DISCUSSIONS

2.3.1 Microstructural study

Figure 2.1 depicts HRTEM images confirming the development of anisotropic MNPs forming isotropic ensembles with a variation in organization. As observed in Figure 2.1(a)–(c), nanorods, with 4±2 nm size, are comprised of maintaining space among MNPs, and resulting in an average of 270 nm sized for CEZF. In Figure 2.1(b), the compact ensemble is shown in yellow mark and Figure 2.1(c), nanorods are highlighted using yellow arrows. Ostwald Ripening mechanism is the ensemble formation mechanism and nanorod growth is governed by the Oriented Attachment (OA) mechanism. While the solvothermal reaction period is increased, the MNPs accumulated on the surface of the ensemble and a hollow interior is evolved and the system is addressed as HCEZF, following the "inside-out Ostwald ripening" growth mechanism [51]. In Figure 2.1(d)-(f), HCEZF shows 6±2 nm average size of for MNPs having a diameter of 270 nm for the ensemble. The MNPs are accumulated on the surface which is confirmed by the observed dark contrast, as shown in yellow arrows in Figure 2.1(e). However, the lighter contrast confirms the hollow interior of HCEZF. The yellow arrows as

depicted in Figure 2.1(f) are due to anisotropic nanorods residing on the surface of HCEZF.

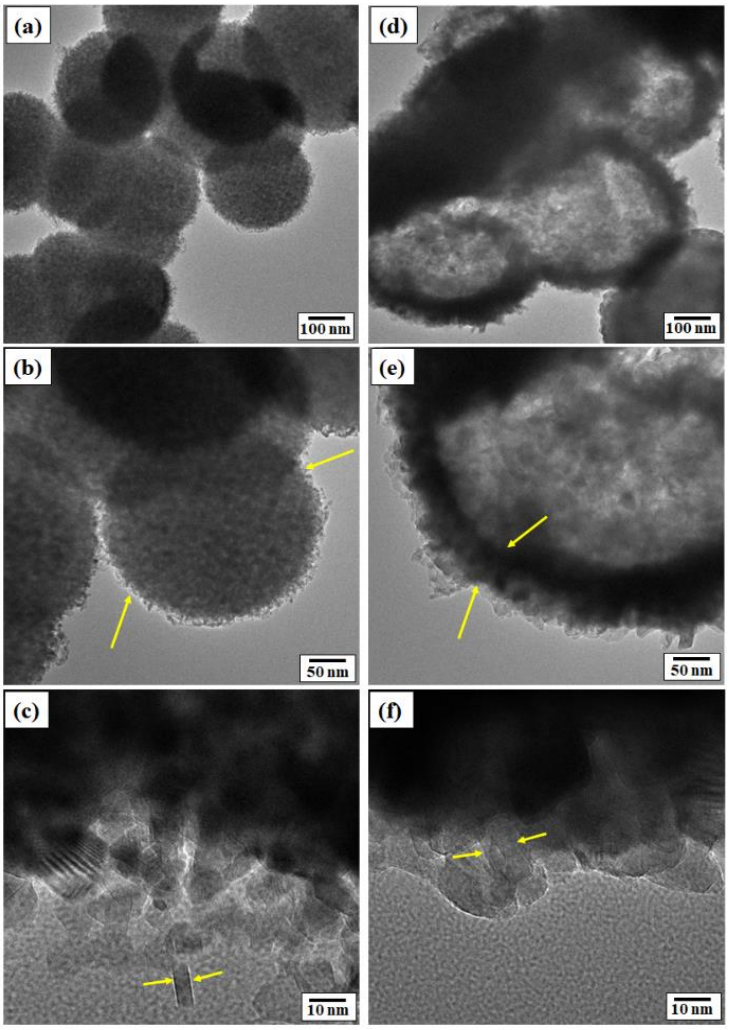

Figure 2.1: Transmission Electron Microscopy (TEM) images of (a, b) Compact Ensemble of Zinc Ferrite (CEZF) and (d, e) Hollow Core Ensemble of Zinc Ferrite (HCEZF), HRTEM images of (c) Compact Ensemble of Zinc Ferrite (CEZF) and (f) Hollow Core Ensemble of Zinc Ferrite (HCEZF). (The nanorods are indicated with yellow arrows in both (c) and (f)). The yellow arrows in Figure (b) indicate the ensemble of CEZF. The yellow arrows in Figure (e) indicate the nanorods assembled on the surface of the ensemble in HCEZF.

In Figure 2.2(a) and 2.2(b), XRD plot is shown in which structural phase and crystalline behaviour are confirmed. The marked diffraction peaks (220), (311),

(400), (511), and (440) are exactly matching with cubic spinel phase of $ZnFe_2O_4$ having JCPDS no. of 82-1042, confirming pure zinc ferrite phase [50]. With increase in reaction period, crystalline property enhancement is depicted in HCEZF. It is because the nanocrystals get enough time to follow the nucleation and growth, resulting in the packing of crystals along with highly ordered arrangement.

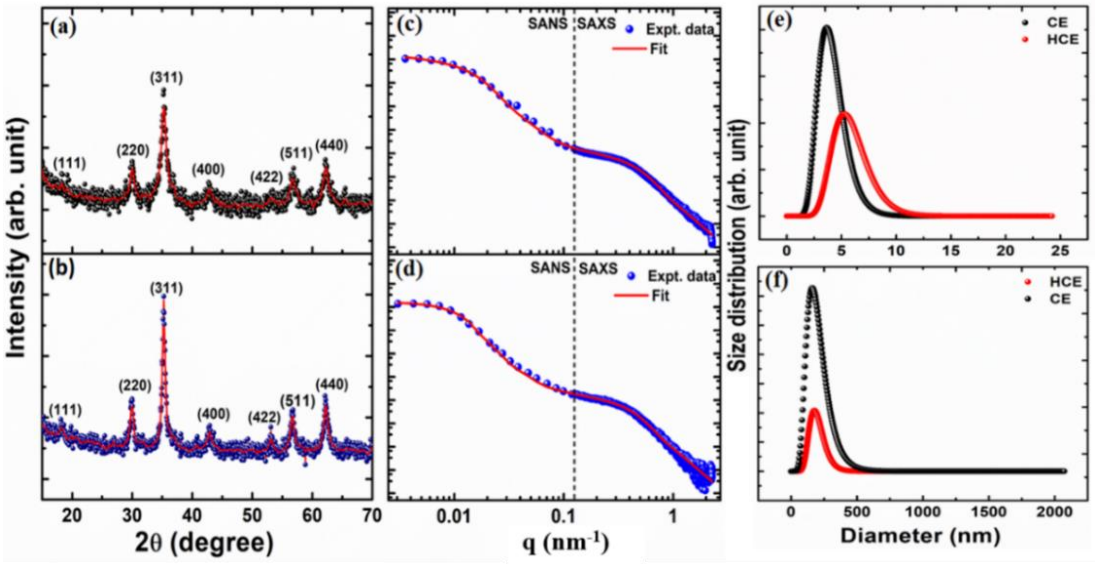

Figure 2.2: XRD profile of (a) CEZF, (b) HCEZF; SAXS and MSANS intensity profiles of (c) CEZF, (d) HCEZF; MNPs size distribution curve of CEZF (black) and HCEZF (red) in (e) primary MNPs from SAXS, and (f) secondary ensembles achieved from MSANS.

For structural analysis, SAXS and MSANS profile plots are shown in Figures 2.2(c) and 2.2(d) for both CEZF and HCEZF to achieve entire microstructural information. The intensity profiles achieved from SAXS analysis are fitted by a cylindrical scattering model, that provides structural correlation of constituent MNPs [52]. The log-normal distribution is considered for intensity fitting of SAXS and MSANS. The considered cylindrical form factor having q as a wave vector with Bessel function J_1 of first order having radius of MNPs R, and length of MNPs 'L' can be addressed as:

$$P(q,R,L) = 4.\int_0^1 \frac{J_1^2}{\left[qR(1-x^2)^{\frac{1}{2}}\right]} \times \frac{[1-cos\,2(qLx/2)]}{2(qLx/2)^2}\,dx \qquad (2.1)$$

The high scattering intensity region (low q region) as shown in Figures 2.2(c) and 2.2(d) are because of the accumulation of MNPs. The higher q area of the SAXS profile gives an idea about the interacting nature of primary MNPs and can be evaluated with a structure factor consideration. Herein, scattering for cylindrical primary MNPs is demonstrated by considering a sticky hard-sphere structure-factor having different fitting parameters for both systems.

However, MSANS profiles as depicted in Figure 2.2(c) and 2.2(d) are fitted by considering a spherical model form factor:

$$P(q,R) = 4\pi R^3\eta[\frac{sin(qR)-qR\,cos(qR)}{(qR)^3}] \qquad (2.2)$$

After performing the fitting, the information regarding morphologies for primary MNPs and secondary ensembles supports HRTEM images. MNPs size distribution curves for both individual MNP and ensembles are displayed in Figures 2.2(e) and 2.2(f). Nonetheless, a slight change in net MNPs size and distance among MNPs can be described through the fact that SAS can inform the detail about overall length, while HRTEM images give detail of a particularly considered length scale only. Herein, scattering data confirm the existence of a sticky hard-sphere (SHS) interaction having packing fraction (φ) of 0.20 and 0.32 for the systems CEZF and HCEZF, accordingly. The rest of the fitting parameters, for example, polydispersity index (σ), MNPs diameter (D), MNPs length (L), and spacing between MNPs (r_i), achieved from, are shown in Table 2.1. The low stickiness, τ, for the system CEZF ~ 0.09, compared to the system HCEZF ~ 0.070, signifies the compactness of HCEZF.

Table 2.1 Fitting values achieved via both SAXS and MSANS fitting.

System	Primary nanoparticles				Secondary structure from MSANS	
	σ	D (nm)	L (nm)	r_i (nm)	D (nm)	σ
CEZF	0.220	4.20	15.980	2.50	190.20	0.230
HCEZF	0.240	5.60	19.50	1.00	193.50	0.250

2.3.2 Direct Current (DC) Magnetization study

To evaluate the dominance of interaction in the systems, remanence curves are analysed which rely on the irreversible magnetization rotation. MNPs with interparticle interaction can be addressed via δM plots. However, Isothermal remanent magnetization (IRM) as well as direct current demagnetization (DCD) conditions are considered to evaluate δM plots, as depicted in Figure 2.3(a). However, for measurement of IRM, the system is demagnetized completely and kept for cooling without considering any external field. Once the needed temperature is reached, a tiny field is provided. Afterwards, the imposed field is turned off and respective remanence values are recorded. Following increasing field, the aforementioned protocol is replicated till the system attains saturation, giving saturated remanence value. Additionally, for DCD curve measurement, a tiny amount of field is imposed considering a reverse direction into the saturated system, at a certain temperature. Then, the moment is measured once the field is switched off, and procedure is continued until a saturation state is attained in reverse direction. The magnetization decay is depicted as a function of the applied field and a correlation between IRM and DCD plots is drawn at 5 K till a field of 2.0 T.

In the case of single-domain MNPs with a noninteracting state having uniaxial anisotropy, the Wohlfarth expression can be used to correlate the IRM and DCD values as:

$$m^{DCD}(H) = 1 - 2m^{IRM}(H) \tag{2.3}$$

Herein m^{DCD} and m^{IRM} address reduced magnetization achieved in DCD and IRM. As per the Stoner- Wohlfarth model [1,2,53], Eq. (2.3) results in a straight line. If deviation from linearity occurs, then the system is dominated by interacting MNPs. To further examine the deviations, the δM plot can be addressed as:

$$\partial M = m^{DCD}(H) - [1 + 2m^{IRM}(H)] \tag{2.4}$$

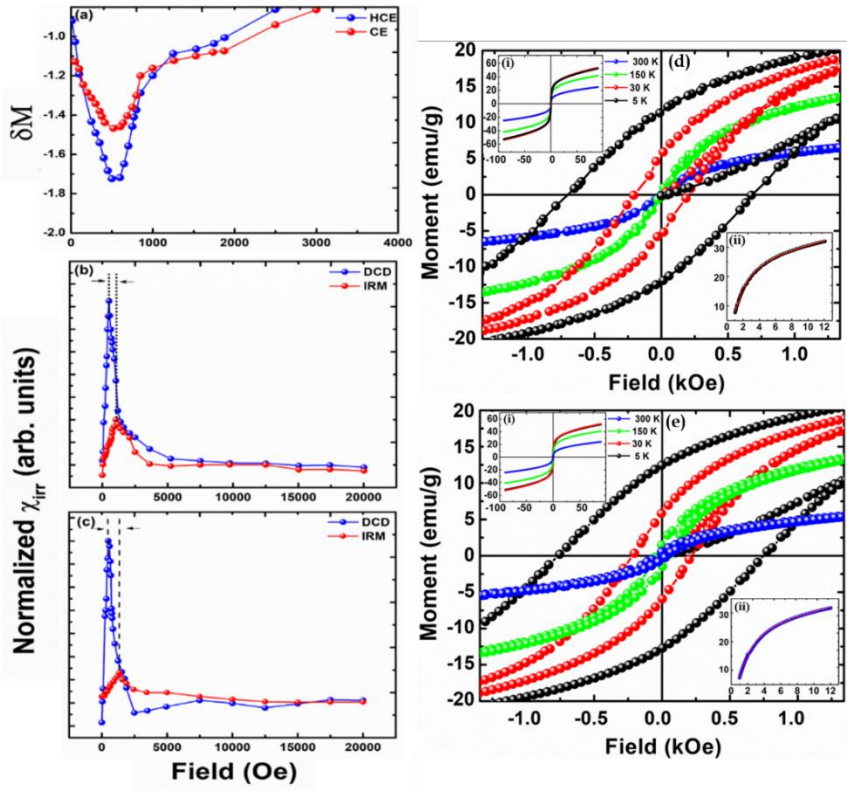

Figure 2.3: (a) δM curves of CEZF and HCEZF, (b, c) Irreversible susceptibility curves: (b) CEZF and (c) HCEZF; Zoomed view of field-dependent magnetization: (d) CEZF and (e) HCEZF. Inset (i): Field-dependent

magnetization of (d) CEZF and (e) HCEZF. Inset (ii): Law of Approach to Saturation (LAS) fitting of (d) CEZF and (e) HCEZF at 5 K.

As the negative deviation in δM plots is achieved in our considered systems as shown in Figure 2.3(a), it reveals the possible dominance of dipolar or demagnetizing interaction among MNPs [1,2]. However, HCEZF depicts more deviation in δM, further confirming the dominance of higher dipolar interaction compared to CEZF. Additionally, after performing differentiation of normalized DCD and IRM plots, distribution of energy barrier can be achieved as depicted in Figures 2.3(b) and 2.3(c). If the remanence curves at a similar reverse field are considered, then irreversible susceptibility (χ_{irr} = dM/dH) is written as:

$$\left|\frac{\partial m^{DCD}}{\partial H}\right| = 2\,\frac{\partial m^{IRM}}{\partial H} \tag{2.5}$$

To get the magnitude of demagnetizing interaction, H_{int}, the mean interaction field can be calculated as [1,2,54]:

$$H_{int} = \frac{1}{2}\,(H_r - H_r^*) \tag{2.6}$$

Herein H_r and H_r^* address the peak positions of field derivatives curves of IRM and DCD. The achieved values of H_{int} are -0.25 kOe and -0.45 kOe for CEZF and HCEZF, as observed in Figure 2.3(b, c). The obtained negative sign signifies the predominance of demagnetizing interaction, further correlating the achieved negative deviation of δM plots. The obtained higher H_{int} magnitude for HCEZF confirms the dominance of stronger demagnetizing interaction, compared to CE, as a consequence supporting the achieved δM plots. As in CEZF, MNPs in their ensembles are arranged to maintain interparticle spacing, and MNPs can flip freely in a certain orientation. In HCEZF, MNPs are accumulated on the surface and are arranged in closer proximity. Hence, dipolar interaction is increasing in HCEZF having closed MNPs, compared to CEZF. However, exchange interaction contribution in such ensembles should not be ignored. We perform a more in-

detail investigation on the collective magnetic nature in these ensembles as given in the next part.

In Figure 2.3 (d, e), the field relying magnetization (M-H) curve is shown with temperatures: 300 K, 150 K, 30 K, and 5 K. The observed '*S*' shaped curves in the M-H condition give the possible existence of disordered states, which are SG state, cluster SG, interacting SPM state, etc. [1,2]. At 300 K, magnetic isotherm depicts narrow hysteresis having a coercivity value of $H_c \sim 37.80$ Oe for HCEZF and $H_c \sim 10.50$ Oe for CEZF. At the lowest temperature of 5 K, H_c~690.0 Oe for CEZF and~759.0 Oe for HCEZF are evaluated. As observed, a higher coercivity value is seen in HCEZF even if HCEZF has higher dipolar strength. Generally, strong demagnetizing interaction makes the magnetic reversal process easier, leading to the low value of coercivity [2], but in current scenario, a stronger demagnetizing field leads to highly energetic valleys of energy landscape. As a result, high thermal energy is required to overcome the high energy barriers. Moreover, saturation is not achieved in the magnetization curve, which may be due to the spin canting of the systems because of the existence of lattice strain and spin frustration [1]. Hence, to calculate anisotropy constant, magnetization data at 5 K are fitted with the aid of the "law of approach to saturation" (LAS) [55] model considering 1000 Oe < H < 12000 Oe range:

$$M = M_S \left[1 - \frac{A}{H} - \frac{B}{H^2}\right] + \kappa H \tag{2.7}$$

Herein, H gives the applied field and $\frac{A}{H}$ is magnetic hardness, ascribing structural defect. $\frac{B}{H^2}$ gives magneto-crystalline anisotropy, from which cubic anisotropy constant K and free space permeability μ_0 can be achieved considering, $B = \frac{8}{105}\frac{K^2}{M_S^2 \mu_0^2}$. κ gives forced magnetization value. The respective fitted curves are depicted in insets of (ii) of Figure 2.3(d) and Figure 2.3(e). The anisotropy constant, K is measured at 5 K and achieved as 7.5×10^4 erg/cm^3 for CEZF and 8.0×10^4 erg/cm^3 for HCEZF. HCEZF shows a higher anisotropy constant,

compared to CEZF. Such high anisotropy is because of the highly competitive complex energy landscape. The saturation magnetization is achieved as 29.30 emu/g for CEZF and 29.50 emu/g for HCEZF. The value of reduced remanence (squareness value) is measured at 5 K, SQ = $\frac{M_r}{M_s}$. SQ is achieved as 0.390 for CEZF and 0.420 for HCEZF. Such obtained SQ is less than the ideal value of uniaxial domains, 0.50, confirming dominance of single domain MNPs having uniaxial anisotropy [1,2,55–57]. Such reduced remanence is a consequence of competing intraparticle anisotropy with demagnetizing interaction, resulting in frustrated spins.

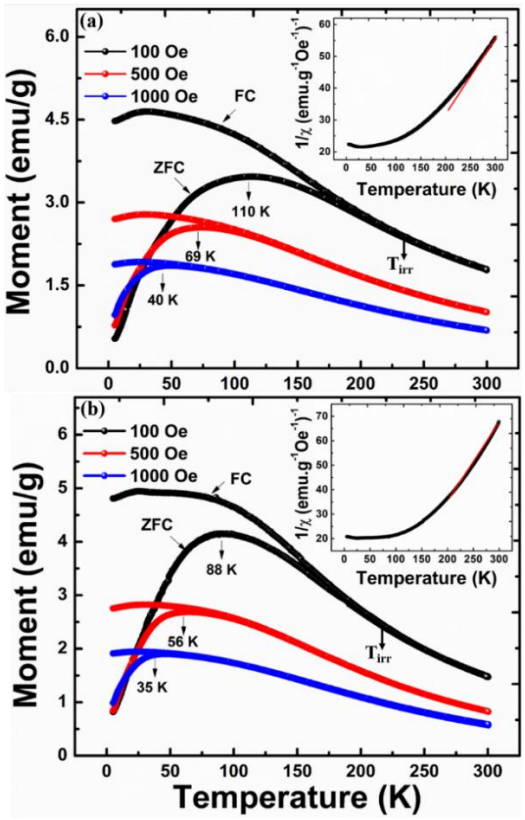

Figure 2.4: Temperature relying magnetization curve: (a) CEZF and (b) HCEZF. Inset gives Curie-Weiss (CW) model fitting.

In Figure 2.4, temperature-dependent magnetization curves at various magnetic fields, including 1000 Oe, 500 Oe, and 100 Oe with the aid of ZFC and FC protocols within 2K–300 K for CEZF and HCEZF. The bifurcation of ZFC-FC

plots below a certain characteristic temperature, T_{irr}, signifies the possibility of the phenomenon of SPM state, spin-glass state, etc. [2]. ZFC curves show broad peaks mentioned as blocking temperature, T_B, at 110 K for the system CEZF and 88 K for the system HCEZF at the field of 100 Oe. T_B values are lower than the obtained 'T_{irr}' for CEZF and HCEZF. This is because of disordered states. For the nature of transition analysis, magnetization is calculated by considering various fields. With an enhanced magnetic field, magnetization decreases, resulting in lower susceptibility. A lowering in T_B value is reflected. With enhanced field strength, anisotropy of the crystal-field is decreased. As a result, high thermal energy is essential to cross energy barriers. If field is low enough, Zeeman energy is less than thermal energy and thermal energy has a pre-dominant role in getting high blocking temperature. HCEZF with high dipolar strength shows low blocking temperature, disagreeing with the DBF model [47,48]. This is because of fast spin relaxation, triggered by an enhanced demagnetizing field. In the achieved FC curves, magnetization saturation is seen below T_B ensuring the strong interaction [1]. With a higher applied field, ZFC and FC moment difference (χ) decreases in the range of low temperature for both CEZF and HCEZF [58]. Hence, T_B shifting with lowering χ, and the behaviour of the FC curve signify the existence of SG transition in the region of low temperature. As given in inset of Figure 2.4, we consider the inverse susceptibility, $1/\chi$, fitting following Curie-Weiss (CW) model [1,2,58] in the region of high-temperature at 100 Oe field:

$$\chi = \frac{C}{T-\theta_{CW}} \tag{2.8}$$

Herein, C gives Curie constant and θ_{CW} is CW temperature. CW law fitting results C ≈ 4.7 g cm^{-3}K and ≈ 3.2 g cm^{-3}K for CE and HCE, and θ_{CW} ≈ 40 K ≈ 88 K for CEZF and HCEZF. The effective magnetic moment is measured considering $\mu_{eff} = \sqrt{3k_B C/N_A}$, Avogadro's number N_A. Hence, μ_{eff} ~ 6.13 μ_B, and ~ 5.06 μ_B for

CEZF and HCEZF are obtained. The positive θ_{CW} signifies the ferromagnetic spin clusters' dominance after a certain transition temperature.

2.3.3 AC susceptibility

To know detail about phase transition behaviour, ac susceptibility is performed in frequency range, 93-9937 Hz, having an ac field of 10 Oe as shown in Figure 2.5. The real component of ac susceptibility, $\chi'(T)$, and imaginary component of ac susceptibility, $\chi''(T)$, as a function of temperature is recorded. Frequency relied significant anomaly is found in $\chi'(T)$ at 160.9 K and 117 K for CEZF and HCEZF, at a certain frequency of 93 Hz and it is addressed as freezing temperature T_f. The variation of T_f with frequency towards a higher range of temperature values and reduced peak height may be because of the spin-glass freezing nature or SPM blocking [1,59]. For further investigation on shifting of T_f with frequencies, the Mydosh parameter [52] is taken as [1,43,58]:

$$k = \Delta T_f / T_f \, (\Delta \, log_{10} f) \tag{2.9}$$

For the calculation of *k*, outermost frequencies such as υ_1 = 93 Hz and υ_1 = 9937 Hz are considered. In the case of a noninteracting SPM system, *k* varies in 0.1-0.28. However, for interacting SPM or spin-glass systems, *k* lies from 10^{-2} to 10^{-3}. Here, *k* gives 0.029 and 0.032 for CEZF and HCEZF. *k* is in higher order than generally reported canonical SG, but in cluster SG range where *k* varies in the range of 0.01-0.09 [1,58]. Hence, the system frequency dependent anomaly is because of spin freezing of randomly arranged interacting magnetic clusters.

Moreover, imaginary part, $\chi''(T)$, as shown in the inset, Figure 2.5, is losses of irreversible domain wall movement, having various relaxation times and giving idea an about the absorption of energy. $\chi''(T)$ peak shifting is reflected in the higher temperature range with enhanced frequency for both CEZF and HCEZF.

To evaluate the nature of disordered magnetic state, the Arrhenius model is used which is valid for noninteracting or weakly interacting particles, and = frequency dependent T_f is fitted following [51,58]:

$$\tau = \tau_0 \exp\left[\frac{E_a}{k_B T_f}\right] \tag{2.10}$$

Herein, τ is dynamical fluctuation having $t_{obs} = 1/2\pi\upsilon$, τ_0 is relaxation period of two consecutive attempts. $\frac{E_a}{k_B}$ gives activation energy, that gives energy barrier separation of respective metastable states. The ln (τ) versus T_f curve fitting is depicted in insets (i) of Figure 2.6(a) and 2.6(b) gives the unphysical parameters for τ_0 and $\frac{E_a}{k_B}$, such as τ_0 = 1.74 × 10^{-34} s and 6.9 × 10^{-32} s for HCE and Ea/k_B = 113 93 K for CEZF and 7627 K for HCEZF. The unphysical values discard the non-interacting SPM state and signify the possible collective nature.

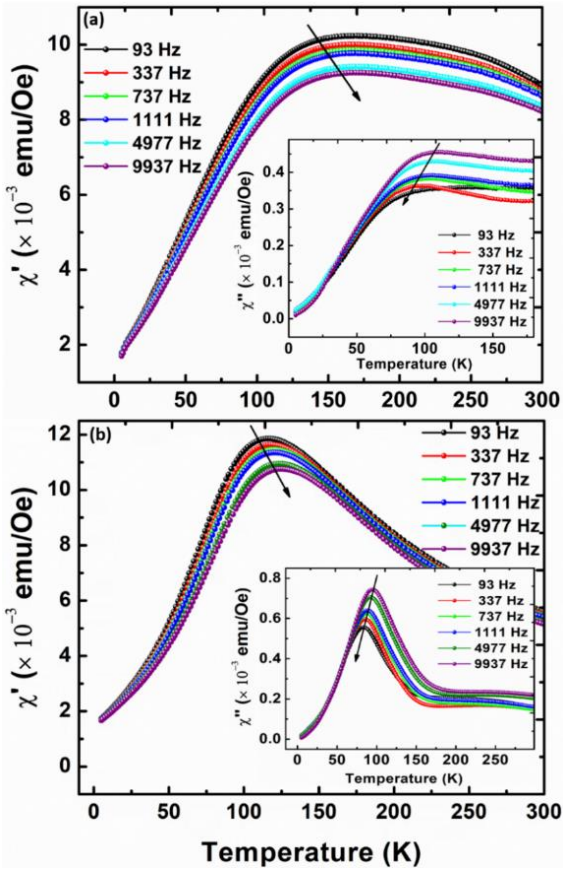

Figure 2.5: Real component ac susceptibility at H_{dc} = 0 kOe and H_{ac} = 10 Oe. Inset gives imaginary component ac susceptibility: (a) CEZF, (b) HCEZF. The arrow mark indicates the change in T_{max} and χ_{max} with an increase in frequency.

Hence, a dynamical scaling law, Vogel Fulcher (VF) model, is addressed as [2, 43]:

$$\tau = \tau_0 \exp\left[\frac{E_a}{k_B(T_f - T_0)}\right] \quad (2.11)$$

Herein, T_0 is the characteristics temperature to get the idea of interparticle interaction and for simplification of fitting of T_f, Eq. (2.11) can be addressed as:

$$\ln \tau = \ln \tau_0 + \frac{E_a}{k_B(T_f - T_0)} \quad (2.12)$$

In the insets (ii) of Figure 2.6(a) and Figure 2.6(b), the fitting of ln τ vs. T_f is shown to have the best linear fit values as, $\tau_0 = 8.8 \times 10^{-9}$ s and 3.8×10^{-10} s for CEZF and HCEZF, and T_0 = 142.5 K and 309.1 K for CEZF and HCEZF, and Ea/k_B = 216 K and 309.1 K for the CEZF and HCEZF. The nonzero T_0 confirms the contribution of definite spin interaction among MNPs. The observed τ_0 is under the characteristic relaxation period for the systems having cluster SG state [1, 55, 60, 61]. HCEZF shows slower relaxation as compared to CEZF, which is the reflection of stronger interaction strength among MNPs. The activation energy is found as $Ea/k_B \sim 1.5T_0$ and $\sim 3.1T_0$ for CEZF and HCEZF. In general, T_0 can be addressed to confirm the coupling strength in the spin clusters, as condition $\frac{E_a}{k_B} >> T_0$ is for weak interaction and the condition $\frac{E_a}{k_B} << T_0$ is because of stronger interaction. A contradictory reflection is observed herein, as HCEZF with a higher interactive nature shows a reverse trend as compared to CE. However, CEZF has activation energy in atomic spin glass range with $\frac{E_a}{k_B} < 2T_0$. Additionally, HCEZF shows higher activation energy. Such enhanced energy is

seen in various reported cluster SG systems, in which collective spin freezing happens due to superspin moments and SG clusters [53,62].

Further, dynamic critical slowing is addressed by considering dynamic scaling theory:

$$\tau = \tau^* \left[\frac{T_f - T_g}{T_g}\right]^{-zv'} \tag{2.13}$$

Where τ* is single spin flip time, T_g gives glass transition temperature, and z is dynamic critical exponent with a critical exponent of v' for correlation length. However, correlation length can be represented as $\zeta = \left(T_f/T_g - 1\right)^{-v'}$ and respective spin-relaxation can be compared to ζ following $\tau \propto \zeta^z$. To fit T_f, the respective power law [Eq. (2.13)] can be represented as:

$$\log(\tau) = \log(\tau^*) - zv' \log\left(\frac{T_f - T_g}{T_g}\right) \tag{2.14}$$

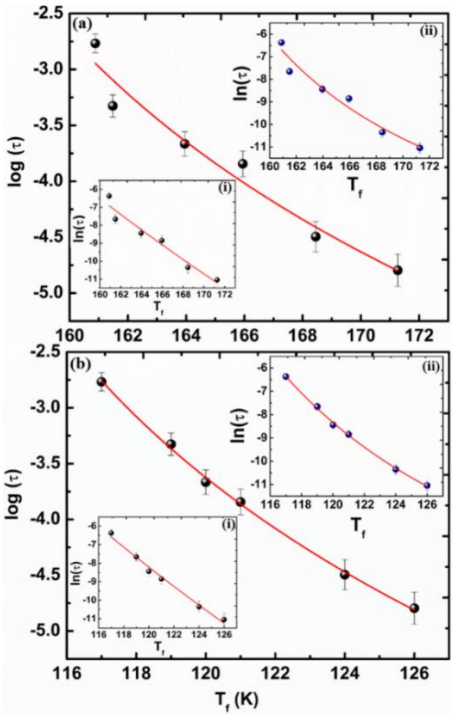

Figure 2.6: (a) Critical slowing down model fitting of CEZF, (b) Critical slowing down model fitting of HCEZF. In inset (i): Arrhenius law of (a) CEZF and (b)

HCEZF, and inset (ii): VF model fitting of (a) CEZF and (b) HCEZF. (The error bars in the data represent standard deviation in experimental data).

As shown in Figure 2.6(a) and Figure 2.6(b) for CEZF and HCEZF, a linear fitting following log(τ) versus T_f is considered. The fitting gives $\tau^* = 7.70 \times 10^{-11}$, $zv' = 6.20 \pm 1.1$ having Tg = 150.40 K for CEZF, and $\tau^* = 1.30 \times 10^{-10}$ s and $zv' = 6.30 \pm 0.5$ with Tg = 108.90 K for HCEZF. In a conventional SG system, zv' and τ^* lie in the 4-12 range and 10^{-10}-10^{-13} s range [41, 53, 63]. In case of canonical SG system, τ^* lies in 10^{-12} and 10^{-13} s range and cluster SG, τ^* lies in 10^{-7} - 10^{-11} s range

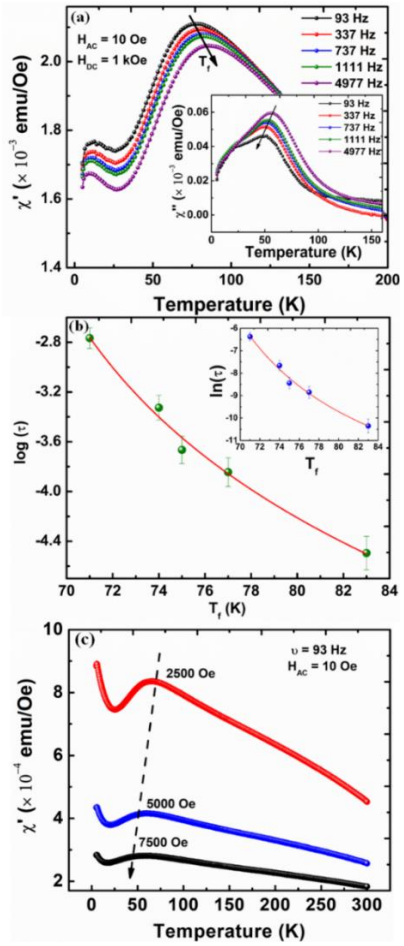

Figure 2.7: (a) Real component ac susceptibility at a field of H_{dc} = 1 kOe and H_{ac} = 10 Oe; inset gives imaginary component ac susceptibility, (b) Power law; inset gives VF model fitting. (c) Real component ac susceptibility at different fields for HCEZF. The arrow mark in Figure (a) indicates the change in T_{max} and χ_{max} with

an increase in frequency and Figure (c) indicates the change in T_{max} with applied DC field. The error bars in the data represent standard deviation in experimental data.

[1, 43, 56, 63]. The fitted values lie in the cluster SG range for both cases. A dc field of H_{dc} = 1 kOe is additionally performed for HCEZF with an ac field of 10 Oe, as depicted in Figures 2.7(a) and 2.7(b). With the dc field, T_f starts to shift towards low-temperature region as seen in $\chi'(T)$ trend [depicted in Figure 2.7(a)]. Above T_f, an inclination of $\chi''(T)$ towards zero is addressed as a typical characteristic of SG state. The fitted parameters are varied in the VF law [Eq. (2.12)] as well as in power law [Eq. (2.14)] [fitting trend is depicted in Figure 2.7(b)]. VF law fitting gives the values of $\tau_0 = 1.6 \times 10^{-7}$, T_0, = 55 K, and Ea/k_B = 145.5 K; and power law gives $\tau*$ and zv′ as 2.8×10^{-7} and 3.7. A lower value in activation energy at condition H_{dc} = 1 kOe is found as compared to activation energy achieved at H_{dc} = 0 condition. A variation in values of $\tau*$ and zv′ is observed, but still lies in the typical range of cluster SG state. The effect of the highly anisotropic nature of HCEZf is further validated with various dc fields as shown in Figure 2.7(c). With dc fields, non-negligible peaks are reflected with slight peak broadening, which confirms SG ground state existence. The SG-transition temperature is shifting to a low-temperature region, confirming the highly anisotropic nature in HCEZF.

The trend of τ can be evaluated by validating dynamic scaling laws. A slight variation is seen between $\tau*$ and τ_0 from both the model, but residing in a similar range for cluster SG [1, 42–44, 58, 64]. The Tholence criterion $\delta T_{Th} = (T_f - T_0)/T_f$ is considered [65] to estimate the degree of magnetic clustering. δT_{Th} is calculated as ≈ 0.1 and ≈ 0.2 for CEZF and HCEZF, validating cluster SG systems range [58]. As δT_{Th} in HCEZF is twice as compared to CEZF, confirming the existence of higher magnetic clustering strength in HCEZF with a stronger demagnetizing effect. The observations of ac susceptibility study provide information on spin dynamics dependency on geometric organization and respective demagnetizing

interactions in ensembles. The cluster SG state is arising in both the cases below T_f. The system HCEZF shows slower spin relaxation with the aid of higher activation energy. With SG state and variation in activation energy, various ergodic nature can be understood. To perform the effect of demagnetizing fields with the aid of organization pattern, the ergodic natures of spin relaxation can be further evaluated by considering MME studies.

2.3.4 Nonequilibrium dynamics

2.3.4.1 Magnetic Memory Effect

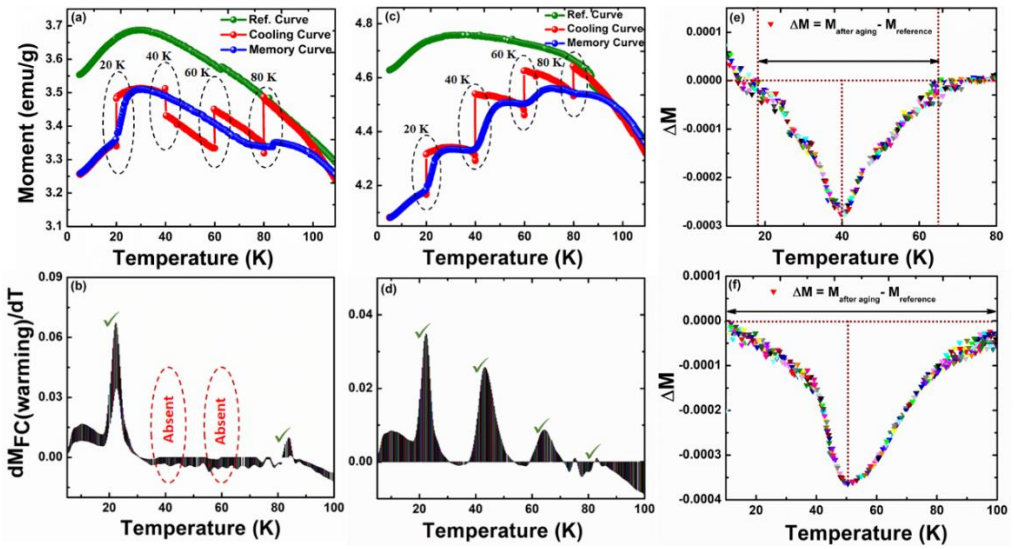

Figure 2.8: Field Cooling Magnetic Memory Effects for: (a) of CEZF and (c) HCEZF, (b, d) derivative curve of FC warming plots: (b) CEZF and (d) HCEZF. (e, f) ZFC MME of (e) CEZF and (f) HCEZF. The elliptical shapes indicate the halted temperature region in (a) and (c). The right tick represents the existence of the memory effect. The arrow marks in (e) and (f) indicate the ΔM region.

For the execution of nonergodicity in spin dynamics, magnetic memory effect (MME) analysis is executed following FC and ZFC conditions [21,22,28]. The FC MME is depicted in Figure 2.8(a)–2.8(d). For FC MME condition, temperature-dependent magnetization is employed to achieve a reference curve. Further, systems are considered to cool till 5 K in 100 Oe field. Four different intermittence

stops are provided at temperatures 80.0 K, 60.0 K, 40.0 K, and 20.0 K in a waiting time of 1 h. At individual stop temperature, if field is off, moments relax towards low-energy configuration. Due to moment relaxation, a decrease in magnetization in each stoppage is found. A steplike behaviour is seen at each stop. After that, probe field is turned on and FC process is considered. The cooling plot having stoppage is addressed as a cooling curve. Once 5 K is attained, moment starts to follow a warming trend up to 300 K at 100 Oe field without further stop and the plot is addressed as a memory plot. If earlier spin identification is memorized by the systems, the MME is said to be found. Here, CEZF can recognize two pronounced MME at 20 K and 80 K. But, HCEZF recognizes all four steps of MME imprints. However, the differentiation of MME plots with respect to temperature, as addressed in Figures 2.8(b) and 2.8(d), gives the presence of a memory step for further confirmation. From the recorded memorized steps, systems can recover the configurations of energy, that are present during thermal cooling.

MME is also performed in ZFC condition, at a certain temperature of 40 K, which is below achieved freezing temperature, having a field of 50 Oe. Generally, SG system shows a nonequilibrium trend and a sufficiently large period is essential to get an equilibrium state [24,25,29]. At first, the general ZFC protocol is done at 50 Oe field to get reference plot, $M_{ref,ZFC}$. Then, the systems are considered for cooling till a temperature of 40 K, with no magnetic field and kept for ageing for a period of 10^4 s. After that, further cooling is executed till 5 K. At this time, warming is performed with a 50 Oe field and moment is calculated till 300 K. The warming curve is addressed as $M_{mem,ZFC}$. An evaluation among the memory plot and respective ZFC reference plot gives a significant memory dip in the perturbed range for both CEZF and HCEZF as shown in Figures 2.8(e) and 2.8(f). It is a result of the cluster SG state, as dynamics of moments are slowed down under a definite temperature. The achieved nonzero ΔM ($M_{mem,ZFC} - M_{ref,ZFC}$) in the range ≈ 10 -50 K, ≈ 10-100 K for CEZF and HCEZF. The systems become

relaxed to their steady dynamics in the waiting period, as addressed in SG models, known as, hierarchical energy [66], and droplet model [67]. In droplet model, domain of compact spins evolved because of excitation occurring in SG state. The nonequilibrium trend of spin aids increases in droplet volume with an increase in time. In ageing, if the temperature is consistent with no perturbation, then the growth of droplets occurs. As a result, the frozen energy barrier is evolved with further cooling and once the warming begins, the frozen energy barrier can be recovered. Low magnetization moments happen during memory path $M_{mem,ZFC}$ with respect to $M_{ref,ZFC}$ because of the flipping nature of energetically excited clusters during warming at perturbed temperature period. The observed wider nonzero ΔM in HCEZF is because of higher frozen energy barriers. For overcoming evolved complex energy landscape, a very high activation energy is needed. The achieved ZFC-FC MME is because of randomly arranged free-energy barriers with a collective nature related to evolved frustrated spins. The modification in MME is seen between the considered systems with no disorderness in the crystalline phase of zinc ferrite. Rather, because of the organization of MNPs, such modifications are observed.

Additionally, ageing relaxation with ZFC protocol is performed as depicted in Figure 2.9 [20]. The cooling of the systems is done till 30 K (T_1) and kept for ageing for 5000 s (t_1) with 50 Oe field. Ageing is the signature identity of the jagged nature of spins in the SG state. If the moments find difficulties in achieving equilibrium conditions, the slowing of spins towards the applied field direction happens following a logarithmic inclination, as depicted in Figures 2.9(a) and 2.9(b) and addressed as "Ageing." Later, a temporary cooling is introduced to 20 K (T_2), and the respective moments are calculated for 7000 s (t_2). The spin dynamics are inconsistent with the dynamics observed during T_1, and moments are found to be arrested and become consistent in this period. The spins are trying to adjust at T_2 without following a slower dynamic. While the temperature is back to T_1, the respective moments are following the ascending relaxation pattern

following its preceding value. Therefore, the systems can memorize significantly the ageing nature at T_1. The respective moment continuity is seen in combined curves [depicted in Figure 2.9(c) and 2.9(d)], signifying complete freezing between the range of 20 K to 30 K. With enhancement in temperature, small-scale spin clusters start to freeze, giving an ageing signal and large spin clusters are blocked, resulting MME nature [28].

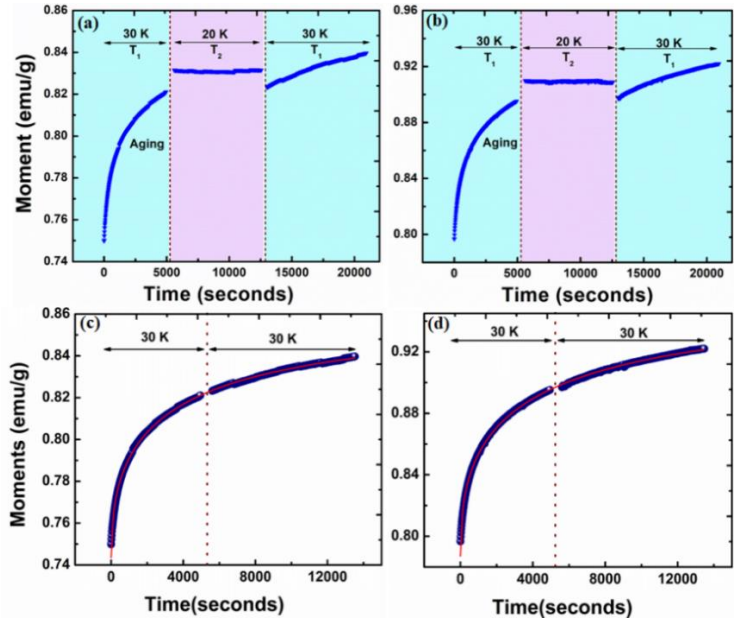

Figure 2.9: (a, b) Ageing relaxation trend with Zero Field Cooling condition for (a) CEZF and (b) HCEZF. (c, d) ageing relaxation continuation with stretched exponential model fit of (c) CEZF and (d) HCEZF.

The observed continuity curves represented in Figure 2.9(c) and 2.9(d) are considered to be fitted with the aid of the stretched exponential function:

$$M(t) = M_0 - M_g exp\left[-\left(\frac{t}{\tau}\right)^{\beta}\right] \quad (2.16)$$

Wherein, M_0 and M_g are intrinsic magnetization and respective glassy component magnetization. τ is for characteristic relaxation period constant. β is for stretching exponent and a function of temperature with a value between 0 and 1. If β = 0, then it is addressed in no spin relaxation. If β provides unity, spin

relaxation is considered to occur with a single time constant. If systems have uniformly arranged energy barriers, the β=1, and 0<β<1 results in possible existence of energy barrier distribution. Herein β is found as 0.47 and 0.45 for CEZF and HCEZF and lies in the range of glassy systems [20, 41, 63]. As β of HCEZF is more as compared to CEZF, hence HCEZF tends to overcome higher anisotropic energy barriers.

Herein, interparticle interaction is found to have a dominant nature to get a complex landscape having an enhanced degree of freedom. Even HCEZF shows a higher demagnetization effect, enhancement in coercivity, and a lower range of freezing temperature with pronounced MME is achieved as compared to CEZF. The achieved outcomes contradict both DBF and MT models. These contradictory natures can overcome by addressing significant modulation of spin dynamics with spatial arrangement in easy axes and dipolar strength through relative geometric variation. For further elucidation, the degree of easy axis alignment is executed with FC magnetization condition as [2, 68]:

$$\frac{M_{Fc}^{align}}{M_{FC}} = 1 + \alpha\,(3\,cos^2\beta - 1) \tag{2.17}$$

In this equation 2.17, α is partially aligned easy axes fraction and β gives respective angle among applied field and easy axes. In systems with high random easy axes, α shows zero value, and then, $\frac{M_{Fc}^{align}}{M_{FC}}$= 1. In case of possible alignment in easy axes, a non-unity value of $\frac{M_{Fc}^{align}}{M_{FC}}$ is observed. For $\frac{M_{Fc}^{align}}{M_{FC}}$ calculation, HCEZF is considered as possessing aligned easy axes and CEZF is considered as randomly oriented easy axes dominated system. At 10 K, $\frac{M_{Fc}^{align}}{M_{FC}}$is calculated as 1.1. The non-unity value confirms the existence of partially aligned easy axes in HCEZF and existence of random easy axes in CEZF [68].

In CEZF, anisotropic MNPs are distributed in random directions with arbitrarily arranged easy axes having less competing energy landscape. The partial alignment in magnetic easy axes with a higher degree of dipolar strength is dominated in HCEZF as represented in the schematic Figure 2.10. In HCEZF, the longer synthesis period allows the primary nanosystems to certain directions around their easy axes before settling on the surface. This leads to partially aligned easy axes with stronger interparticle strength. The complex energy barrier in such a competing system leads to magnetic frustration. Hence, besides demagnetizing strength, distinction in the geometric pattern of MNPs and easy axes arrangement can modify dynamic magnetic behaviour.

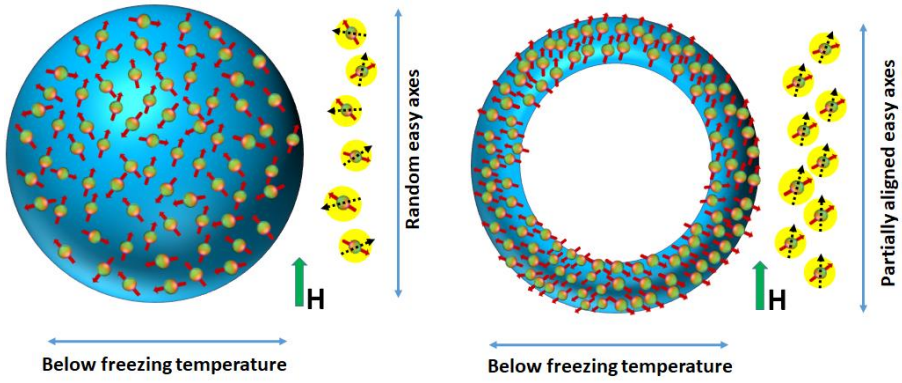

Figure 2.10: Schematic presentation of easy axis in CEZF (left) and HCEZF (right).

2.4 CONCLUDING REMARKS

The dynamic magnetic nature is revealed for two differently organized identical systems CEZF and HCEZF having different geometry. The dominance of demagnetizing strength triggers low temperature SG state. The existence of moderately aligned easy axes as well as a competing landscape of anisotropic energy in HCEZF trigger coercive field enhancement with enhanced demagnetizing field and low blocking temperature. Additionally, Mydosh parameter as well as Tholence criterion support the evolution of cluster SG state in both cases. Enhanced activation energy with broadening energy barriers, FC/ZFC MME, and ZFC ageing reflect cluster SG state establishment. With the

hollow geometric arrangement in HCEZF having competitive pinned spins yields enhanced magnetic anisotropy with enhanced FC-MME and wider ΔM in ZFC-MME, as compared to CEZF. This chapter states slower spin dynamics with modulation in MME with various geometric arrangements of anisotropic MNPs, degree of demagnetizing field, as well as easy axes alignment.

References

[1] Bhattacharya, K., V. Dupuis, V., Roy, D. Le and Deb, P. Progressive freezing of interacting spins in isolated finite magnetic ensembles. *Journal of Physics: Condensed Matter,* 29:045002, 2017.

[2] Saikia, K., Sarma, D. D. and P. Deb, Organization dependent collective magnetic properties of secondary nanostructures with differential spatial ordering and magnetic easy axis orientation. *Journal of Magnetism and Magnetic Materials,* 408:127, 2016.

[3] Iglesias O. and Labarta, A. Magnetic relaxation in terms of microscopic energy barriers in a model of dipolar interacting nanoparticles. *Physical Review B,* **70**:144401, 2004.

[4] Sánchez, F. H., Zélis, P. M., Arciniegas, M. L., Pasquevich, G. A. and Raap, M. B. F. Dipolar interaction and demagnetizing effects in magnetic nanoparticle dispersions: Introducing the mean-field interacting superparamagnet model. *Physical Review B,* 95:134421, 2017.

[5] Jamet, M., Wernsdorfer, W., Thirion, C., Dupuis, V., Melinon, P., Perez, A. and Mailly, D. Magnetic anisotropy in single clusters. *Physical Review B,* 69:024401, 2004.

[6] Y. Sun, M. B. Salamon, K. Garnier, and R. S. Averback, Memory effects in an interacting magnetic nanoparticle system. *Physical Review Letters,* 91:167206 (2003).

[7] Thakur, M., Patra, M., Majumdar, S. and Giri, S. Coexistence of superparamagnetic and superspin glass behaviors in $Co_{50}Ni_{50}$ nanoparticles embedded in the amorphous SiO_2 host. *Journal of Applied Physics,* 105:073905 (2009).

[8] Chen, X., Bedanta, S., Petracic, O., Kleemann, W., Sahoo, S., Cardoso, S. and Freitas, P. P. Superparamagnetism versus superspin glass behavior in dilute magnetic nanoparticle systems. *Physical Review B,* 72:214436, 2005.

[9] Bedanta, S., Eimuller, T., Kleemann, W., Rhensius, J., Stromberg, F., Amaladass, E., Cardoso, S. and Freitas, P. P. Overcoming the dipolar disorder in dense CoFe nanoparticle ensembles: Superferromagnetism. *Physical Review Letters,* 98:176601, 2007.

[10] Bandyopadhyay M. and Dattagupta, S. Memory in nanomagnetic systems: Superparamagnetism versus spin-glass behavior. *Physical Review B*, 74:214410, 2006.

[11] Pramanik, A. K. and Banerjee, A. *Physical Review B,* 82:094402, 2010.

[12] Karmakar, S., Chaudhuri, B. K., Chan, C. L. and Yang, H. D. Origin of low temperature memory and aging effects in spin glass like $La_{0.7}Ca_{0.3}MnO_3$ nanomanganite. *Journal of Applied Physics,* 108:113916, 2010.

[13] Dupuis, V., Vincent, E., Bouchaud, J.-P., Hammann, J., Ito, A. and Katori, H. A. Aging, rejuvenation, and memory effects in Ising and Heisenberg spin glasses. *Physical Review B*, 64:174204, 2001.

[14] Bedanta, S. and Kleemann, W. Supermagnetism. *Journal of Physics D,* 42: 013001, 2009.

[15] Markovich, V., Fita, I., Wisniewski, A., Jung, G., Mogilyansky, D., Puzniak, R., Titelman, L. and Gorodetsky, G. Spin-glass-like properties of La0.8Ca0.2MnO3 nanoparticles ensembles. *Physical Review B*, 81:134440, 2010.

[16] Hiroi, K., Komatsu, K. and Sato, T. Superspin glass originating from dipolar interaction with controlled interparticle distance among γ-Fe_2O_3 nanoparticles with silica shells. *Physical Review B,* 83:224423, 2011.

[17] Suzuki, M., Fullem, S. I., Suzuki, I. S., Wang, L. Y. and Zhong, C. J. Observation of superspin-glass behavior in Fe_2O_3 Nanoparticles. *Physical Review B,* 79:024418, 2009.

[18] Nayek, C., Samanta, S., Manna, K., Pokle, A., Nanda, B., Kumar, A. and Murugavel, P. Spin-glass state in nanoparticulate $(La_{0.7}Sr_{0.3}MnO_3)_{1-x}(BaTiO_3)_x$ solid solutions: Experimental and density-functional studies. *Physical Review B,* 93:094401, 2016.

[19] Yin, H. and Chakraborty, B. Slow dynamics and aging in a nonrandomly frustrated spin system. *Physics Review E,* 65:036119, 2002.

[20] Khan, N., Mandal, P. and Prabhakaran, D. Memory effects and magnetic relaxation in single-crystalline $La_{0.9}Sr_{0.1}CoO_3$. *Physical Review B,* 90:024421, 2014.

[21] Sasaki, M., Jönsson, P. E., Takayama, H. and Mamiya, H. Aging and memory effects in superparamagnets and superspin glasses. *Physical Review B,* 71:104405, 2005.

[22] Kundu, A. K., Nordblad, P. and Rao, C. N. R. Nonequilibrium magnetic properties of single-crystalline $La_{0.7}Ca_{0.3}CoO_3$. *Physical Review B,* 72:144423 (2005).

[23] Parker, D., Dupuis, V., Ladieu, F., Bouchaud, J.-P., Dubois, E., Perzynski, R. and Vincent, E. Spin-glass behavior in an interacting γ-Fe2O3 nanoparticle system. *Physical Review B,* **77**:104428, 2008.

[24] Sahoo, S., Petracic, O., Kleemann, W., Nordblad, P., Cardoso, S. and Freitas, P. P. Aging and memory in a superspin glass. *Physical Review B,* 67:214422, 2003.

[25] Vasilakaki, M., Trohidou, K. N., Peddis, D., Fiorani, D., Mathieu, R., Hudl, M., Nordblad, P., Binns, C. and Baker, S. Memory effects on the magnetic behavior of assemblies of nanoparticles with ferromagnetic core/antiferromagnetic shell morphology. *Physical Review B,* **88**:140402(R), 2013.

[26] Chakraverty, S., Bandyopadhyay, M., Chatterjee, S., Dattagupta, S. Frydman, A., Sengupta, S. and Sreeram, P. A. Memory in a magnetic nanoparticle system: polydispersity and interaction effects. *Physical Review B,* 71:054401, 2005.

[27] Chatterjee, S., Giri, S., Majumdar, S. and De, S. K. Metastability and magnetic memory effect in $Ni_2Mn_{1.4}Sn_{0.6}$. *Physical Review B,* 77:012404, 2008.

[28] Rodriguez, G. F., Kenning, G. G. and Orbach, R. Full aging in spin glasses. *Physical Review Letters,* **91**:037203, 2003.

[29] Scalliet, C. and Berthier, L. Rejuvenation and memory effects in a structural glass. *Physical Review Letters,* 122:255502, 2019.

[30] Maity, T., Goswami, S., Bhattacharya, D. and Roy, S. Superspin Glass Mediated Giant Spontaneous Exchange Bias in a Nanocomposite of $BiFeO_3-Bi_2Fe_4O_9$. *Physical Review Letters,* 110:107201, 2013.

[31] Tian, Z., Xu, L., Gao, Y., Yuan, S. and Xia, Z. Magnetic memory effect at room temperature in exchange coupled $NiFe_2O_4$-NiO nanogranular system. *Applied Physics Letters,* 111:182406, 2017.

[32] Du, J., Zhang, B., Zheng, R. K. and Zhang, X. X. Memory effect and spin-glass-like behavior in Co-Ag granular films. *Physical Review B,* 75:014415, 2007.

[33] Cabot, A., Alivisatos, A. P., Puntes, V. F., Balcells, L., Iglesias, O. and Labarta, A. Magnetic domains and surface effects in hollow maghemite nanoparticles. *Physical Review B,* 79:094419, 2009.

[34] Quintero-Castro, D. L., Lake, B., Reehuis, M., Niazi, A., Ryll, H., Islam, A. T. M. N., Fennell, T., Kimber, S. A. J., Klemke, B., Ollivier, J., Sakai, V. G., Deen, P.

P. and Mutka, H. Coexistence of long- and short-range magnetic order in the frustrated magnet $SrYb_2O_4$. Phys. Rev. B **86**:064203, 2012.

[35] Khurshid, H., Li, W., Phan, M.-H., Mukherjee, P., Hadjipanayis, G. C. and Srikanth, H. Surface spin disorder and exchange-bias in hollow maghemite nanoparticles. *Applied Physics Letters,* 101:022403, 2012.

[36] Anand, V. K., Opherden, L., Xu, J., Adroja, D. T., Hillier, A. D., Biswas, P. K., Herrmannsdörfer, T., Uhlarz, M., Hornung, J., Wosnitza, J., Canévet, E. and Lake, B. Evidence for a dynamical ground state in the frustrated pyrohafnate $Tb_2Hf_2O_7$. *Physical Review B,* 97:094402, 2018.

[37] Kozelj, P., Jazbec, S., Vrtnik, S., Jelen, A., Dolinsek, J., Jagodic, M., Jaglicic, Z., Boulet, P., Weerd, M. C. de, Ledieu, J., Dubois, J. M. and Fournee, V. Geometrically frustrated magnetism of spins on icosahedral clusters: The $Gd_3Au_{13}Sn_4$ quasicrystalline approximant. *Physical Review B,* 88:214202, 2013.

[38] Gardner, J. S., Gingras, M. J. P. and Greedan, J. E. Magnetic pyrochlore oxides. *Reviews of Modern Physics,* 82:53, 2010.

[39] Nath, R., Tsirlin, A. A., Kaul, E. E., Baenitz, M., Buttgen, N., Geibel, C. and Rosner, H. Strong frustration due to competing ferromagnetic and antiferromagnetic interactions: Magnetic properties of $M(VO)_2(PO_4)_2$ (M=Ca and Sr). *Physical Review B,* 78:024418, 2008.

[40] Crespo, Y., Andreanov, A. and Seriani, N. Competing antiferromagnetic and spin-glass phases in a hollandite structure. *Physical Review B,* 88:014202, 2013.

[41] Pakhira, S., Mazumdar, C., Ranganathan, R., Giri, S. and Avdeev, M. *Physical Review B,* 94:104414, 2016.

[42] Vera Stimpson, L. J., Powell, J. M., Stenning, G. B. G., Jura, M. and Arnold, D. C. Spin-glass behavior in KxRu4−yNiyO8 hollandite materials. *Physical Review B,* 98:174429, 2018.

[43] Kroder, J., Manna, K., Kriegner, D., Sukhanov, A. S., Liu, E., Borrmann, H., Hoser, A., Gooth, J., Schnelle, W., Inosov, D. S., Fecher, G. H. and Felser, C. Spin glass behavior in the disordered half-Heusler compound IrMnGa. *Physical Review B,* 99:174410, 2019.

[44] Sahoo, R. C., Takeuchi, Y., Ohtomo, A. and Hossain, Z. Exchange bias and spin glass states driven by antisite disorder in the double perovskite compound $LaSrCoFeO_6$. *Physical Review B,* **100**:214436, 2019.

[45] Kumar, A., Senyshyn, A. and Pandey, D. Evidence for cluster spin glass phase with precursor short-range antiferromagnetic correlations in the B-site disordered $Ca(Fe_{1/2}Nb_{1/2})O_3$ perovskite. *Physical Review B,* 99:214425, 2019.

[46] Vlášková, K., Colman, R. H., Proschek, P., C˘apek, J. and Klicpera, M. Evidence for spin-glass ground state in fluorite-defect $Er_2Zr_2O_7$ single crystals. *Physical Review B,* 100:214405, 2019.

[47] Dormann, J. L., Bessais, L. and Fiorani, D. A dynamic study of small interacting particles: superparamagnetic model and spin-glass laws. *Journal of Physics C: Solid State Physics,* 21:2015, 1988.

[48] D. Fiorani, J. Dormann, R. Cherkaoui, E. Tronc, F. Lucari, F. Dorazio, L. Spinu, M. Nogues, A. Garcia, and A. M. Testa, Collective magnetic state in nanoparticles systems. *Journal of Magnetism and Magnetic Materials,* 143: 196, 1999.

[49] Morup, S. and Tronc, E. Superparamagnetic relaxation of weakly interacting particles. *Physical Review Letters,* 72:3278, 1994.

[50] Zhou, X., Li, H., Sun, X., Sun, P., Liang, X., Liu, F., Hu, X. and Lu, G. Nanosheet-Assembled $ZnFe_2O_4$ Hollow Microspheres for High-Sensitive Acetone Sensor. *ACS Applied Materials Interfaces,* 7:15414, 2015.

[51] Truong, A., Watanabe, A. O., Mortemousque, P. A., Ando, K., Sato, T., Taniyama, T. and Itoh, K. M. Interfacial spin-glass-like state in Mn_5Ge_3 single

crystalline films grown on germanium substrates. *Physical Review B,* 91:214425, 2015.

[52] Engel, M., Stuhn, B., Schneider, J. J., Cornelius, T. and Naumann, M. Small-angle X-ray scattering (SAXS) off parallel, cylindrical, well-defined nanopores: from random pore distribution to highly ordered samples. *Applied Physics A*, 97(A):99, 2009.

[53] Wohlfarth, E. P. Relations between different modes of acquisition of the remanent magnetization of ferromagnetic particles. *Journal of Applied Physics*, 29:595, 1958.

[54] Laureti, S., Varvaro, G., Testa, A. M., Fiorani, D., Agostinelli, E., Piccaluga, G., Musinu, A., Ardu, A. and Peddis, D. Magnetic interactions in silica coated nanoporous assemblies of $CoFe_2O_4$ nanoparticles with cubic magnetic anisotropy. *Nanotechnology,* 21:315701, 2010.

[55] Herbst, J. F. and Pinkerton, F. E. Law of approach to saturation for polycrystalline ferromagnets: Remanent initial state. *Physical Review B,* 57:10733, 1998.

[56] Geshev, J., Viegas, A. D. C. and Schmidt, J. E. Negative remanent magnetization of fine particles with competing cubic and uniaxial anisotropies. *Journal of Applied Physics,* 84:1488, 1998.

[57] Ibusuki, T., Kojima, S., Kitakami, O. and Shimada, Y. Magnetic anisotropy and behaviors of Fe nanoparticles, *IEEE Transactions on Magnetics*, 37:2223, 2001.

[58] P. Bag, P. R. Baral, and Nath, R. Cluster spin-glass behavior and memory effect in $Cr_{0.5}Fe_{0.5}Ga$. *Physical Review B,* 98:144436, 2018.

[59] Gangopadhyay, S., Hadjipanayis, G. C., Dale, B., Sorensen, C. M., Klabunde, K. J., Papaefthymiou, V. and Kastikas, A. Magnetic properties of ultrafine iron particles. *Physical Review B,* 45:9778, 1992.

[60] Mydosh, J. A. Spin glasses: redux: an updated experimental/materials survey. *Reports on Progress in Physics,* 78:052501, 2015.

[61] Vijayanandhini, K. Simon, C., Pralong, V., Caignaert, V. and Raveau, B. Spin glass to cluster glass transition in geometrically frustrated $CaBaFe_{4-x}Li_xO_7$ ferrimagnets. *Physical Review B,* 79:224407, 2009.

[62] Kechrakos, D. and Trohidou, K. N. Magnetic properties of dipolar interacting single-domain particles. *Physical Review B,* 58: 12169, 1998.

[63] Ghara, S., Jeon, B.-G. Yoo, K., Kim, K. H. and Sundaresan, A. Reentrant spin-glass state and magnetodielectric effect in the spiral magnet $BiMnFe_2O_6$. *Physical Review B,* 90:024413, 2014.

[64] Chandra, S. Khurshid, H., Li, W. Hadjipanayis, G. C. Phan, M. H. and Srikanth, H. Spin dynamics and criteria for onset of exchange bias in superspin glass $Fe/\gamma\text{-}Fe_2O_3$ core-shell nanoparticles. *Physical Review B*, 86:014426, 2012.

[65] Tholence, J.-L. Recent experiments about the spin-glass transition. *Physica B,* 126:157, 1984.

[66] Sibani, P. and Hoffmann, K. H. Hierarchical models for aging and relaxation of spin glasses. *Physical Review Letters*, 63:2853, 1989.

[67] Fisher D. S. and Huse, D. A. Equilibrium behavior of the spin-glass ordered phase. *Physical Review B,* 38:386, 1988.

[68] Ngo, A. T. and Pileni, M. P. Assemblies of ferrite nanocrystals: partial orientation of the easy magnetic axes. *The Journal of Physical Chemistry B,* 105:53, 2001.